JOURNAL OF GEOPHYSICAL RESEARCH, VOL. 104, NO. C9, PAGES 20,753–20,766, SEPTEMBER 15, 1999

Ocean wave height determined from inland seismometer data: Implications for investigating wave climate changes in the NE Pacific

Peter D. Bromirski
Center for Coastal Studies, Scripps Institution of Oceanography, University of California, San Diego, La Jolla

Reinhard E. Flick
California Department of Boating and Waterways, Center for Coastal Studies, Scripps Institution of Oceanography, University of California, San Diego, La Jolla

Nicholas Graham
Climate Research Division, Scripps Institution of Oceanography, University of California, San Diego, La Jolla

Abstract. Knowing the wave climate along the California coast is vital from the perspectives of climatological change and planning shore protection measures. Buoy data indicate that the wave climate is very similar along much of the California coast. We show that elements of the wave climate can be accurately reconstructed using near-coastal inland broadband seismometer data. Such reconstructions are possible because swell approaching the coast generates pressure fluctuations that are locally transformed into seismic waves at the seafloor that propagate inland and are detectable by land-based seismometers. Buoy and seismometer data show that most of the microseism energy recorded inland near the coast is generated from wave events at nearby coastal locations. A site-specific, empirically derived seismic-to-wave transfer function is demonstrated to be applicable to seismic data from the same location for any year. These results suggest that ocean wave heights estimated from near-coastal broadband seismometer data are sufficiently reliable for monitoring the coastal wave height when buoy data are unavailable, provided that adequate simultaneous nearby buoy measurements are available to calibrate the seismometer data. The methodology presented here provides an important tool that allows the investigation of potential wave climate changes from reconstructions using archived seismic data collected since the 1930s.

1. Introduction

The severe 1997-1998 winter storm cycle in the North Pacific, with its damaging effects on the California shoreline, has focused attention on the variability of the wave climate along the California coast. Specifically of interest is the comparison of the wave climate of the current El Niño-Southern Oscillation (ENSO) along the West Coast not only with that of the 1982-1983 episode, but also with earlier El Niño related wave cycles. Unfortunately, the record of long-term buoy measurements of waves along the West Coast is rather short, beginning in the early 1980s. Consequently, the instrumental wave record prior to the availability of buoy and satellite data is very incomplete, making unreliable the quantitative comparisons between recent buoy measurements and the wave record from earlier periods. Historical reconstructions of extreme-wave episodes and their climatologies must therefore generally be developed using marine meteorological analyses and are hence subject to considerable uncertainty. It is important to reduce this uncertainty, since reconstructions of extreme-wave episodes along the West Coast are important for coastal engineering and shore processes studies and also because they are relevant to possible changes in the incidence and/or intensity of extreme storms postulated under scenarios of natural or anthropogenic climate change.

The uncertainty in the wave record is of particular concern because meteorologically based historical reconstructions suggest large fluctuations in the wave climate of the West Coast [*Seymour et al.*, 1984; *Seymour*, 1996], with the majority of the most intense episodes since 1900 occurring after the mid-1970s. In apparent accordance with these findings, recent studies suggest

Paper number 1999JC900156.
0148-0227/99/1999JC900156$09.00

a change in climate in the Northern Hemisphere during the mid-1970s [*Nitta and Yamada*, 1989; *Trenberth*, 1990; *Trenberth and Hurrell*, 1994; *Graham*, 1994; *Born*, 1996]. *Seymour et al.* [1984] investigated the relationship of ENSO to California's wave climate, focusing primarily on the strong 1982-1983 ENSO. The number of large wave events reported by *Seymour* [1996] for the well-recorded, very strong 1982-1983 ENSO is conspicuously larger than the number for the strong, but not well-recorded, 1940-1941 ENSO.

An alternative to using meteorological data to reconstruct the historical wave climate is to use archived analog broadband seismometer data. Such reconstructions are possible because swell approaching the coast generates pressure fluctuations that are locally transformed into seismic waves at the seafloor that propagate inland and are detectable by land-based seismometers located near the coast. The archived seismometer data can potentially extend the complete wave record back several decades.

The purpose of this paper is to demonstrate that the local wave climate can be accurately reconstructed using recent near-coastal inland digital broadband seismometer data. First, we show the reliability of using seismic wave climate reconstructions from the San Francisco Bay area as representative of the wave climate along much of the California coast. The relationship between the ocean wave spectrum and the microseism spectrum allows the estimation of a seismic-to-wave transfer function that enables reconstruction of the ocean wave height and wave period from seismic data. Seismometer and buoy data collected during the 1997-1998 El Niño wave cycle demonstrate the reliability of the methodology and are compared with buoy data from the 1982-1983 El Niño.

2. Buoy Data: Spatial Variation of Wave Parameters

The ocean wave spectrum results both from swell from distant storms and from "sea" generated by local winds. Ocean gravity waves can be characterized by the significant wave height H_s (the height of the highest 1/3 of the waves) and the peak wave period T_P (the wave period with the greatest energy). H_s is computed from the wave spectral density data S_w as $H_s = 4m_0^{1/2}$, where m_0 is the zeroth moment of the wave spectrum, $m_0 = \int S_w(f)df$. Differences in H_s as measured at different coastal locations result from differing storm fetch parameters and local coastal bathymetry, as well as dispersion and spreading effects related to the relative positions of the wave-generating storms.

Extreme wave episodes have a strong impact on the California coast. Wave heights and other wave parameters have been routinely monitored along the California coast since the early 1980s using near-coastal wave measurement buoys. Buoy data from several coastal locations are available from the National Oceanic and Atmospheric Administration (NOAA) National Oceanic Data Center (NODC) CD-ROM data sets. Simultaneous broadband seismometer data are available from the Berkeley Seismological Laboratory for the Berkeley seismic station BKS. Buoys near BKS are NOAA buoys 46026 and 46013, located in coastal waters near San Francisco (Figure 1). Wave reconstructions from these seismic data have local significance because, as shown below, the wave climate measured near San Francisco is representative of the wave climate along much of the California coast; that is, waves from large storms have similar characteristics at coastal buoys separated by hundreds of nautical miles.

To illustrate the spatial homogeneity along the California coast, we show H_s (Plate 1) from coastal NOAA buoys 46013, 46026, 46011, and 46023 from Point Conception to Point Reyes (see Figure 1 for locations) for the November 1, 1982, to February 28, 1983, time period, corresponding to the strongest El Niño related wave episode on record prior to the current ENSO. Water depths at buoys 46013, 46026, 46011, and 46023 are 121, 33, 196, and 623 m, respectively. Plate 1 shows that wave data from the San Francisco coastal area are representative of the wave climate over much of the California coast. Measurements of H_s at these locations are very similar, with the typical difference in H_s (at buoys other than 46026) less than 1.0 m. In particular, the amplitudes of the peaks of H_s correspond closely, with virtually simultaneous peaks at all the coastal buoys. A similar variation in T_P is observed at the same buoys. Differences in H_s, e.g., between 46013 and 46023, result, to a large extent, from their proximity to the wave-generating storms, with buoys farthest from the source areas generally having the largest reduction in amplitude from spreading and dispersion effects. H_s at 46026 (Plate 1, dark blue line) is consistently somewhat less than at the other buoys as a result of being partially sheltered by the Farallon Islands. Consequently, we use unsheltered, deep water buoy 46013 as the reference buoy to calibrate the seismic data below, since local wave energy that does not reach 46026 will generate microseisms that will be detected at BKS.

3. Relating the Ocean Wave Spectrum to the Seismic Microseism Spectrum

Storm winds generate dispersive waves, with long-period waves traveling faster than short periods in deep water. The peak of the ocean wave spectrum for a fully developed sea depends on the maximum sustained wind speed of the storm and the length and duration of the fetch [*Pierson and Moskowitz*, 1964]. As the sustained wind speed increases, the frequency of the peak of the wave spectrum decreases (that is, the peak wave period increases). Swells with peak energy at very low frequencies are generated only by very high sustained wind speeds. Thus the frequency associated with the largest waves gives a conservative estimate of the maximum sustained wind speed of the storm.

Numerous studies have investigated the character-

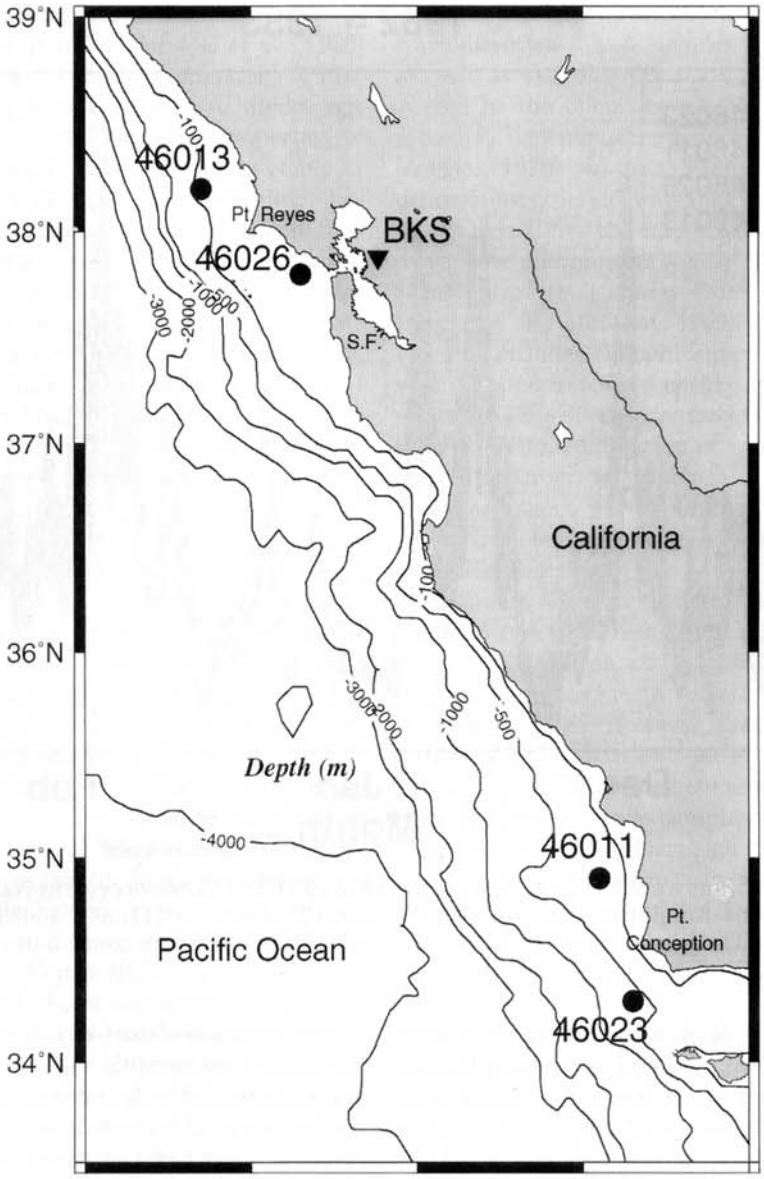

Figure 1. Locations of California coastal buoys (circles) and the Berkeley (BKS) seismometer site (triangle). Bathymetric contours are in meters below sea level.

istics of wave-generated microseism noise (see *Webb* [1998] and *Orcutt et al.* [1993] for reviews). Microseisms have been attributed to swell that has propagated across large stretches of ocean [*Munk et al.*, 1963; *Haubrich et al.*, 1963] as well as to local storm waves that are prominent sources of microseisms in the [0.2,0.5] Hz band [*Babcock et al.*, 1994]. Microseisms result from the conversion of wave-generated signals to seismic energy at the ocean bottom. When swell enters shallow coastal waters, "single-frequency" or primary microseisms at the frequency of the waves are generated. The amplitude of the pressure fluctuations from the ocean waves falls off exponentially with depth below the free surface, with the result that this mechanism is ineffective in generating primary microseisms except in shallow coastal waters. Although not well understood, possible mechanisms for coupling ocean wave energy to the solid earth include the interaction of the ocean wave pressure signal with the sloping seafloor and/or the breaking of waves at the shoreline [*Hasselmann*, 1963]. Primary microseisms from swell arrivals produce a weak spectral peak in the [0.04,0.1] Hz band. The weak coupling between the ocean waves and seismic energy results in the amplitude of primary microseisms being at times below detection levels.

More energetic microseisms that dominate the noise levels in the [0.1,0.5] Hz band are also observed at double the ocean wave frequency. Wave energy is converted to acoustic energy at the sea surface as a result of the interaction of ocean gravity waves with opposing components. The amplitude of these "double-frequency" microseisms is proportional to the product

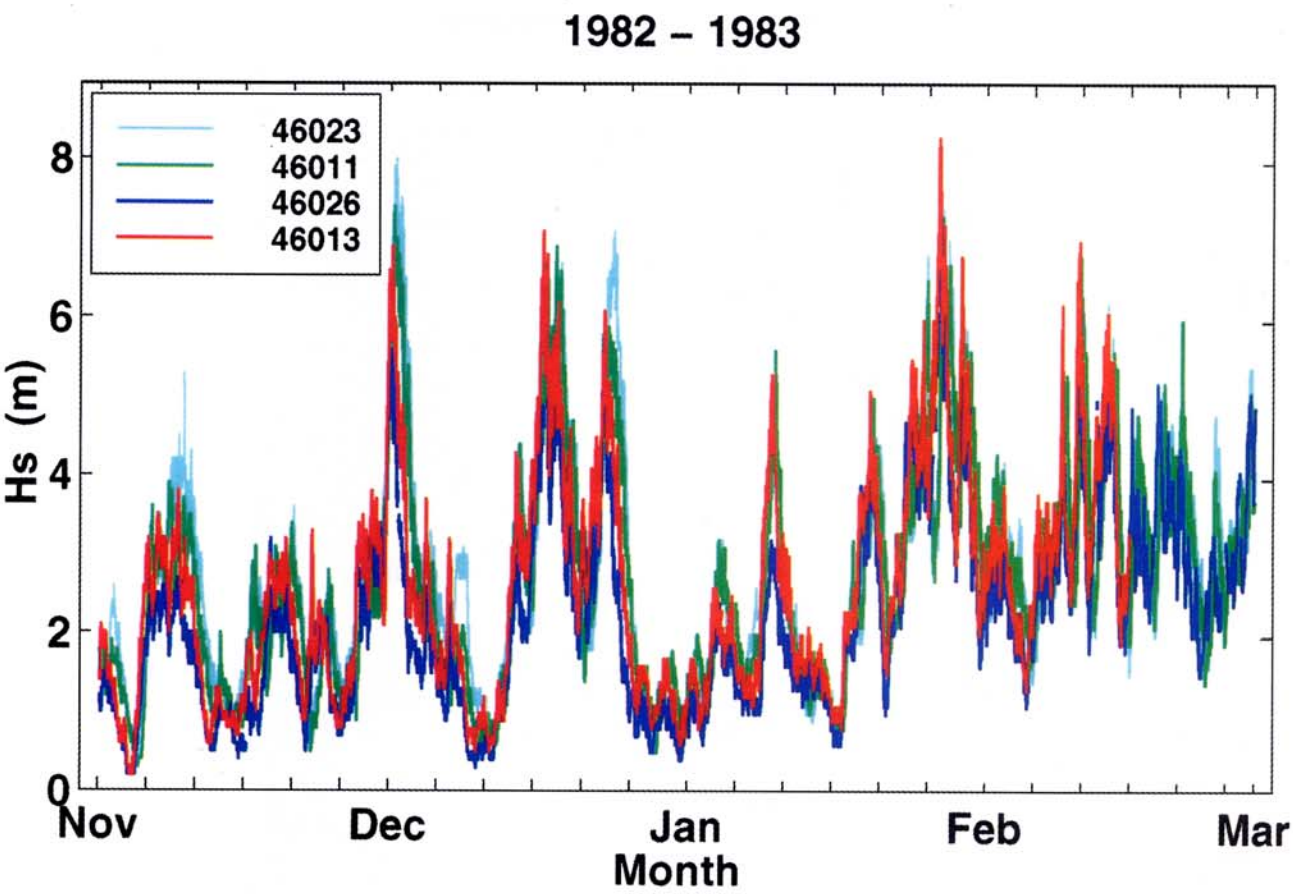

Plate 1. Significant wave height H_s during the 1982-1983 El Niño wave cycle at National Oceanic and Atmospheric Administration (NOAA) buoys 46013, 46026, 46011, and 46023 (see Figure 1 for locations). The legend gives the associated line color. Tick marks are at 5-day increments.

of the amplitudes of the opposing ocean waves producing them [*Longuet-Higgins*, 1950]. In addition to multiple storm systems, opposing waves may occur near the wave generation region as the winds in a storm system vary in direction, or near the coast from the coastal reflection of incident swell [*Haubrich and McCamy*, 1969]. *Munk et al.* [1963] estimated coastal reflection of Southern Hemisphere swell to be about 20% from array measurements off San Clemente Island. *Haubrich et al.* [1963] showed that obliquely arriving Southern Hemisphere swell generates corresponding double-frequency microseisms, suggesting that sufficient opposing reflected wave energy can result from a wide range of nonnormal swell approach angles. From the frequency and relative narrowness of the double-frequency peak of near-coastal seismometer data and neglecting swell refraction and local bathymetric effects, Haubrich et al. estimated that the generation area comprised a coastal strip about 150 km long, centered at the coastal point nearest the seismometer and extending seaward as much as 300 km. *Bromirski and Duennebier* [1998] confirmed from dispersed swell spectra and their associated double-frequency microseisms that wave-wave interaction at nearby coastlines dominates the near-coastal double-frequency microseism spectrum.

The nonlinear nature of interactions between opposing gravity waves with slightly different wavenumbers results in second-order pressure fluctuations with small wavenumbers that propagate to the deep seafloor as acoustic waves having a broad phase velocity spectrum and amplitudes that do not attenuate appreciably with depth. The high-velocity components of the pressure spectrum excite freely propagating body waves, while the low-velocity components excite trapped (surface) waves in the waveguide bounded above by a pressure release surface and below by the large increase in seismic velocities with depth in the oceanic crust [*Hasselmann*, 1963]. A small component of the resulting microseism wave field propagates as compressional or shear body waves, with this energy primarily at frequencies above 0.2 Hz [*Haubrich and McCamy*, 1969]. Although a wide band of surface-wave velocities are excited, the only surface-wave phases that propagate well are those corresponding to the various modes that are characteristic of the ocean-seafloor waveguide [*Webb*, 1992]. These double-frequency microseisms have much higher amplitudes than the primary microseisms whose origins are less clearly understood. Consequently, we use the double-frequency microseism spectrum to reconstruct H_s.

Analysis of microseism particle motion and phase relationships at the ocean floor by *Barstow et al.* [1989] indicates that microseisms are predominately fundamental mode Rayleigh waves. As these modes approach the coast, the rapidly changing properties of the waveguide as the water depth decreases result in the energy in the Rayleigh modes at the seafloor being greatly reduced. *Hasselmann* [1963] showed that refraction of Rayleigh-wave modes propagating toward the shore can significantly reduce the amount of deep-ocean-generated microseism energy reaching near-coastal sites, confirmed by *Haubrich et al.* [1963]. Conversion to body wave phases [*Haubrich and McCamy*, 1963] and scattering into other modes [*Schreiner and Dorman*, 1990] may also be important mechanisms that dissipate open-ocean-generated microseism energy in near-coastal areas. The microseisms observed at near-coastal locations are consequently dominated by conversion of the local wave-induced pressure field into seismic waves that propagate inland. Confirmation of the "local" generation of the near-coastal microseism signal is inferred from the close temporal agreement between the peak frequencies and patterns of ocean swell and microseism spectra, and the narrow width of some microseism peaks in frequency (see Plate 2 and Figure 4).

The measurement or hindcasting of ocean wave height from seismometer data has been used in the past by *Zopf et al.* [1976] to monitor wave conditions on the Oregon coast using a specially designed land-based microseismometer wave measurement system located close to the shore. Recent results from that system are presented by *Tillotson and Komar* [1997]. *Kibblewhite and Brown* [1991] estimated the wave amplitudes on the New Zealand coast using a land-based seismometer, also located near the shore. Below we show that broadband data from seismometers located inland from the coast can also give good estimates of wave height using an empirically derived seismic-to-wave transfer function.

4. Theory

The theory of microseism generation is well established, with a detailed presentation of the wave-wave interaction initially given by *Longuet-Higgens* [1950] and further developed by *Hasselmann* [1963] and many others. An approximate form of the wave-wave pressure excitation spectrum S_P from the nonlinear interaction of opposing waves can be expressed as

$$S_P(\omega_d) = \frac{\pi\rho^2 g^2}{2c^2}\,\omega^3\,S_w^2(\omega)\,\mathcal{W}_\theta(\omega), \qquad (1)$$

where S_w is the gravity-wave spectral density (buoy data) at wave frequency ω, ρ is the ocean surface density of seawater, g is the acceleration due to gravity, c is the ocean sound speed, and the pressure spectrum frequency ω_d is double the wave frequency; that is, $\omega_d = 2\omega$ [see, e.g., *Kibblewhite and Ewans*, 1985; *Webb and Cox*, 1986]. $\mathcal{W}_\theta$ describes the directional properties of the gravity-wave wave field as a function of wave direction θ and includes the opposing wave field as well as the directional properties of the incoming swell. In the open ocean, $\mathcal{W}_\theta$ can be modeled with a $\cos^q(\theta)$ dependence, where q is the beam parameter [*Hughes*, 1976]. In areas where the directional dependence of long-period waves is constrained by proximity to the coastline, the opposing wave field that causes wave-wave microseisms is most likely dominated by the reflection of swell energy from the irregular coastline [*Haubrich and McCamy*, 1969]. In near-coastal regions, $\mathcal{W}_\theta$ also includes the ambient "local-sea" wave field as well as opposing wave energy resulting from trapped waves leaking off the continental shelf and the reflection/refraction/diffraction of wave energy from nearby coastal features. In principal, an estimate of the combined nearshore wave field coefficients $\mathcal{W}_\theta$ can be obtained from buoy (S_w) and hydrophone (S_P) data using a modified version of (1).

In shallow water, a significant contribution to the microseism spectrum results from an amplification factor due to propagation effects associated with the generation of inhomogeneous interface waves [*Schmidt and Kuperman*, 1988]. However, the inhomogeneous contribution to the ocean bottom noise spectrum does not propagate well inland, where the contribution resulting from the homogeneous component of the pressure field dominates the microseism signal and is thus closely associated with the ocean wave height [*Kibblewhite and Brown*, 1991]. In simplified form, the vertical seismic displacement spectrum at the ocean bottom, $S_z(\omega_d)$, can be expressed as

$$S_z(\omega_d) = R_s(\omega)\,T_z(\omega_d)\,S_P(\omega_d), \qquad (2)$$

where R_s represents the local active source region of wave-wave interactions and T_z is the pressure-to-seismic Rayleigh-wave transfer function. Then S_z detected by an inland seismometer can be expressed in terms of the ocean gravity-wave spectral density as

$$S_z(\omega_d) = \frac{\pi\rho^2 g^2}{2c^2}\omega^3 S_w^2(\omega)\Big[R_s(\omega)\mathcal{W}_\theta(\omega)T_z(\omega_d)\alpha_R(\omega_d)\Big]. \qquad (3)$$

The microseism generation area term R_s depends on the wave period and the magnitude and location of the wave-generating storm from the coast (beam width), and T_z will vary over R_s as the the local shelf geology varies. However, since S_z at microseism frequencies is predominantly "locally" generated and since we are primarily concerned with waves having periods greater than 10 s, we assume that the variation in R_s is much less than the variation in S_z levels and that T_z is relatively constant over R_s. For inland sensor locations, attenuation of the Rayleigh-wave microseism signal must also be considered. The attenuation α_R depends both on the geologic structure and the distance between the source area and the seismometer and may be frequency-dependent. More thorough representations of the mi-

croseism excitation theory are given by *Hasselmann* [1963], *Schmidt and Kuperman* [1988], *Kibblewhite and Wu* [1991], *Webb* [1992], and others.

The transfer function Γ_{sw} relates the microseism amplitudes to the ocean wave amplitudes. Prior to estimating Γ_{sw}, the microseism spectral levels must be corrected for the frequency-dependent terms (in brackets in (3)) that modify the wave spectrum characteristics. Each of these terms is difficult to estimate over a variable area for varying source characteristics. An alternative to estimating these terms individually is to determine composite wave-to-seismic coefficients T_{ws} empirically from normalized seismometer data and normalized buoy data for corresponding frequency bands, that is,

$$T_{ws}(\omega_d) = R_s(\omega)\, \mathcal{W}_\theta(\omega)\, T_z(\omega_d)\, \alpha_R(\omega_d) \approx \frac{S_w^2(\omega)/S_w^2(\omega)_{\max}}{S_z^2(\omega_d)/S_z^2(\omega_d)_{\max}}. \quad (4)$$

An advantage of estimating T_{ws} in this manner is that assumptions about R_s, $\mathcal{W}_\theta$, T_z, and α_R are unnecessary.

Converting (3) to temporal frequency f, where $\omega = 2\pi f$, and substituting T_{ws} for the terms in brackets, the equivalent (seismic) gravity-wave spectral density $\hat{S}_w$ is then estimated from

$$\hat{S}_w(f_d) = \left[\frac{S_z(f_d)}{\frac{4\pi^4\rho^2 g^2}{c^2} f^3\, T_{ws}(f_d)} \right]^{\frac{1}{2}}, \quad (5)$$

where f is the ocean gravity-wave spectral density frequency, $f_d = 2f$, and S_z is the vertical displacement seismometer data. Then the equivalent (seismic) significant wave height $\hat{H}_s$ is obtained from the band-limited zeroth moment of the seismic spectrum as

$$\hat{H}_s = 4 \left[\int_{f_1}^{f_2} \hat{S}_w(f_d)\, df \right]^{\frac{1}{2}}, \quad (6)$$

where we choose $f_1 = 0.085$ Hz and $f_2 = 0.48$ Hz. Here, f_1 is selected to exclude most swell-derived primary microseism energy and other ultralong-period noise, and f_2 is limited by the Nyquist frequency of the long-period seismometer data. The corresponding proxy peak wave period, $\hat{T}_p$, is estimated as twice the period of the maximum of $\hat{S}_w(f_d)$.

Since the microseism amplitudes are proportional to the square of the wave amplitudes and also include probable nonlinear contributions from R_s, we use a quadratic least squares fit to a plot of seismic $\hat{H}_s$ versus wave H_s for corresponding time periods to obtain the seismic-to-wave transfer function Γ_{sw}. Estimating Γ_{sw} in this manner averages the frequency and wave height dependent parameters that affect the microseism amplitudes. Γ_{sw} is applied to the $\hat{H}_s$ estimates (Equation (6)) to obtain the proxy wave height $\tilde{H}_s$; that is, $\tilde{H}_s = \Gamma_{sw}\, \hat{H}_s$. Seismometer data containing surface-wave signals from earthquakes, ground shaking attributed to severe local wind conditions, and other sources of significant nonocean-wave-related signals must be excluded when determining Γ_{sw}.

5. Application: Berkeley (BKS) Versus Buoy 46013

Broadband seismometer data have been continuously recorded at the University of California, Berkeley, since about 1930. Digital broadband vertical-component seismometer data decimated to 1 Hz used in this study are available since 1992 from the Northern California Earthquake Data Center (NCEDC) for the Berkeley seismographic station (BKS). Buoy data are available from NODC as previously noted.

5.1. Spectral Characteristics

The spectral energy levels at buoy 46013 and seismic station BKS (see Figure 1 for locations) for January, February, and March 1995 are shown in Plate 2. Tick marks are at 5-day intervals except at the end of each month. Spectral levels above or below the ranges shown were set equal to that respective bound. The 46013 data consist of hourly wave spectral density estimates that result from averaging wave measurements of 1024 s duration [*Steele et al.*, 1985]. The BKS spectral levels were computed from the seismometer time series by averaging three consecutive 512 s data segments with 256 s overlap using standard fast Fourier transform processing with a Hanning window. To reduce the variance in the spectral estimates, each spectral estimate (in dB) was averaged together with the two adjacent spectral estimates at both higher and lower frequencies for each segment prior to averaging the spectral estimates from the three segments. The resulting 14 spectral estimates in each hour were then averaged to obtain hourly seismic estimates corresponding to the buoy data times. Vertical stripes in Plate 2b are either earthquake transients or missing data.

Most of the ocean wave energy is found in the [0.04, 0.20] Hz band (Plate 2a). Locally generated "sea" is typically characterized by significant energy at periods less than 10 s (i.e., at frequencies > 0.1 Hz) and by the peak in the wave energy spectrum initially shifting to lower frequencies (longer periods), indicative of the progressive development of the in-fetch spectrum or the increase in wind speed as the local storm intensity increases [*Bretschneider*, 1959]. The typical local-sea spectral signature is exemplified by the event near March 10, clearly showing a decrease in the frequency of the spectral peak with time. The relationship between local sea development and associated changes in the microseism spectrum has previously been observed by *Kibblewhite and Evans* [1985] and *Babcock et al.* [1994]. In contrast, the arrival of swell from distant storms shows the wave spectral peak shifting from low to high frequencies (shorter periods) as a result of the dispersion of ocean waves in deep water [*Munk et al.*, 1963]. This

increase in peak frequency with time is observed for several dispersed swell arrivals, e.g., on January 22 and March 23, giving a characteristic spectral shape that is observed for other events at both 46013 and BKS.

The similarity in energy concentration between these data sets is clear, with the seismic response at twice the ocean wave frequency (Plate 2b). Energy concentrations at frequencies less than about 0.085 Hz are primary microseisms. The wave-wave double-frequency boundary is easily identified. Note that the highest wave energy levels at 46013 have a close correspondence with the highest microseism levels at BKS. The similarity of relative energy levels is closest for swell events where the wave energy is concentrated in the [0.05,0.08] Hz band. The combination of local sea concurrent with the arrival of swell from one or more storms, e.g., during March 9-11, complicates the spectral signatures. However, these types of simultaneous wave arrivals can still be differentiated in the seismic data. The close temporal correspondence in the spectral energy concentration between 46013 and BKS, i.e., the lack of wave-wave microseisms in the absence of swell energy, confirms that these signals are locally generated.

5.2. BKS-46013 Transfer Function

Average energy spectra for estimating T_{ws} using (4) were obtained from the 95th percentile of the ranked normalized spectral energy estimates for 46013 and BKS from January 1 to January 24, when high wave energy occurred at both long and short periods. The ratio of the average energy at 46013 at wave frequency f to the average BKS energy at microseism double-frequency f_d gives $T_{ws}(f_d)$ (Figure 2). We assume that T_{ws} does not change appreciably with wave amplitude. Since energy at frequencies below the microseism peak is associated with primary microseisms and $T_{ws}(0.12) \approx 1$, we set $T_{ws}(< 0.12) = 1$.

T_{ws} increases with frequency, indicating that the microseism levels at BKS have a relatively lower short-period component compared to the associated wave spectra observed at buoy 46013. The buoy response function decreases with frequency and is not well determined above about 0.35 Hz (K. E. Steele, National Data Buoy Center, personal communication, 1999). However, since the range of T_{ws} shown in Figure 2 corresponds to a maximum wave frequency of 0.25 Hz, the increase in T_{ws} with frequency is probably not related to the buoy response. Alternatively, the increase in T_{ws} with frequency may be related to the reflection characteristics of swell from beaches. Gravity-wave reflection from beaches depends on beach slope, wave height, and wave period, with the ratio of seaward to shoreward propagating energy decreasing with frequency [*Elgar et al.*, 1994]. Consequently, frequency-dependent gravity-wave reflection would result in relatively lower amplitude short-period microseisms and cause an increase in T_{ws} with frequency, provided that shore reflection contributes significantly to the opposing wave field for nearshore microseism generation. Note that T_{ws} includes microseism attenuation between the generation region and the seismometer, also contributing to the increase in T_{ws} as observed.

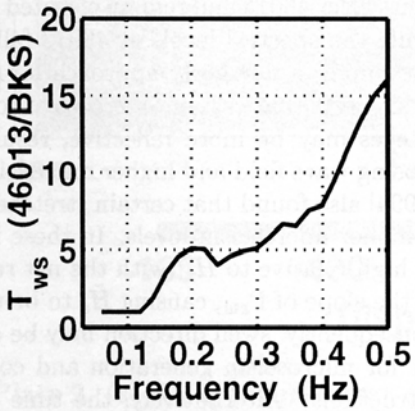

Figure 2. Wave-to-seismic transfer function T_{ws} determined from the ratio of the "average" normalized spectral energy at buoy 46013 to the corresponding average double-frequency energy at seismic station BKS for the January 1-24, 1995, time period.

The T_{ws} estimates were used in (5) to compute $\hat{S}_w$, giving $\hat{H}_s$ in (6). Plotting $\hat{H}_s$ versus H_s for BKS (in the [0.08,0.48] Hz band) and 46013 (in the [0.03,0.38] Hz band), respectively, for corresponding time periods gives the seismic-to-wave transfer function Γ_{sw} (Figure 3a). *Kibblewhite and Evans* [1985] observed similar variation between microseism and ocean wave amplitudes for the New Zealand coast. Although we use the quadratic least squares coefficients (represented by the stippled line in Figure 3a) to obtain $\hat{H}_s$, a linear least squares regression fit to these data has a correlation coefficient R^2 rm of 0.88, indicating that these data are well correlated; and although more stringent constraints on "noise" exclusion would reduce some of the scatter in Figure 3a, tests showed that the reduced $\hat{H}_s$ versus H_s data set did not cause a significant change in the Γ_{sw} inversion results, suggesting that these regression coefficients are relatively stable as indicated by the high R^2.

Although Figure 3a demonstrates a clear relationship between the wave-wave microseism and ocean wave amplitudes, the variance suggests potentially significant error in the seismic reconstruction. That this need not be the case is shown by plotting H_s for January-March 1995 from two relatively nearby ocean buoys that are in R_s, buoys 46013 and 46026 (Figure 3b; see Figure 1 for locations). Recalling that microseism levels result from the summation of signals generated over R_s, Figure 3b shows that the 46026-46013 variance is not greatly different from that between 46013 and BKS. The variance between 46013 and 46026 results from differences in exposure and bathymetry and temporal variation as a result of swell propagation, as well as statistical sampling variability inherent in using 1024 s records. In addition, different wind conditions at these buoys separated by

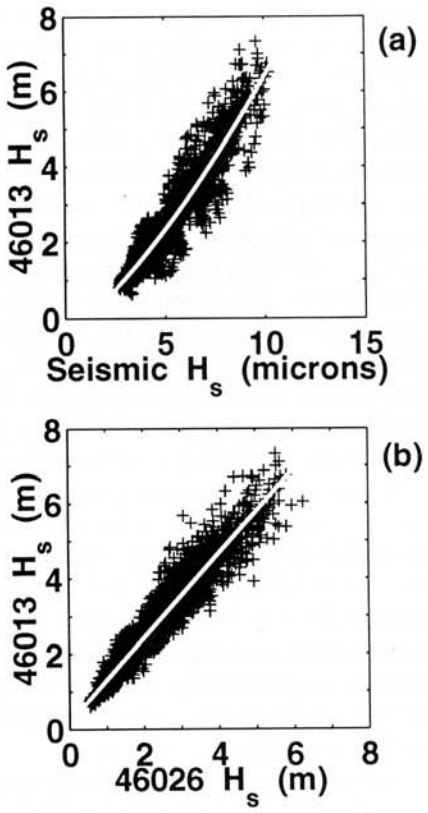

Figure 3. (a) Equivalent (seismic) significant wave height $\hat{H}_s$ from BKS versus buoy 46013 H_s. Stippled line is the quadratic least squares fit to these data and represents the microseism-to-wave transfer function Γ_{sw}. (b) H_s at 46026 versus H_s at 46013 showing the variation in H_s at two nearby coastal buoys (see Figure 1 for locations).

about 80 km causes variability in the short-period wave spectra between 46013 and 46026, resulting in corresponding differences in H_s. The linear least squares fit for 46026 versus 46013 (Figure 3b, stippled line) has an $R^2 = 0.92$, comparable to that for BKS-46013, with a slope of 1.12 that is indicative of the somewhat lower H_s at sheltered buoy 46026. A similar variance, $R^2 = 0.89$, is observed between unsheltered deep water buoys 46011 and 46023 for the same time period, indicating that this amount of variation observed in H_s is common between relatively nearby buoys. Since buoy 46013 is near the northern limit of R_s from BKS as estimated by *Haubrich et al.* [1963] and since the 46026-46013 and 46013-BKS variances are similar, the resulting H_s from reconstructions should show variation similar to that observed between the two buoys.

In addition to the dominant locally generated microseism signals, S_z includes microseism energy from nonlocal wave activity that we will refer to as "telemicroseisms." The telemicroseism level depends on the storm size and its location relative to the coast. To estimate the magnitude of the telemicroseismic contribution at BKS, we compare the spectral characteristics of the peak of the relatively short duration high-amplitude swell event at 46013 and BKS on January 22 in the [0.03,0.2] Hz band (Figure 4) with the lowest levels preceding the swell arrival. Similar relative energy levels and spectral content for the buoy and seismometer data are observed, again showing the one-to-one correspondence between local swell and microseism amplitudes. The peak spectral energy levels at 2100 UT at 46013 (solid line) normalized to the maximum spectral level are shown in Figure 5, with the lower curve from January 22 at 0600 UT using the same normalization as that for the peak energy curve. Curves for the same times from BKS (dashed lines) normalized to the BKS peak energy on January 22 at 2100 UT are also shown in Figure 5. The peak at BKS is nearly twice the wave frequency as predicted by theory. Since virtually no swell energy is observed at 46013 in the [0.03,0.1] Hz band near 0600 UT on January 22, the microseism energy at BKS at that time in the [0.1,0.15] Hz band must be primarily of nonlocal origin. An estimate of the telemicroseism contribution at BKS can be inferred from the lower BKS curve in Figure 5, where the energy at 0.12 Hz is about 10% of the swell event peak at a time when the associated wave energy at 46013 at half that frequency (0.06 Hz) is close to zero. However, part of this apparent telemicroseism energy may result from local wave activity that is not present at 46013. Regardless, Figure 4 shows that microseism levels at BKS correspond closely with nearby wave activity and that telemicroseism energy will not significantly affect the accuracy of H_s reconstructions.

For obliquely arriving swell, the variance in Γ_{sw} partly results from the more rapid variation in wave H_s compared to $\hat{H}_s$; that is, the microseism levels can remain relatively high for longer time periods as a result of wave-wave interactions that generate microseism signals that are local to BKS but occur after the swell passes 46013. In that respect, proxy wave heights $\tilde{H}_s$ are derived from spatial as well as temporal averaging. The seismic amplitudes at BKS in Figure 4b peak about 2 hours after 46013 and remain elevated for nearly 3 hours while the spectral levels at 46013 fall off more rapidly. Assuming a northerly approach for this swell event, this suggests that certain stretches of coast south of Point Reyes may be more reflective, resulting in a larger opposing wave field and higher microseism levels. *Cessaro* [1994] also found that certain stretches of coast generated higher microseism levels. In these instances, $\hat{H}_s$ will be high relative to H_s, with the net result a reduction in the slope of Γ_{sw}, causing $\tilde{H}_s$ to be underestimated. Consequently, swell direction may be an important factor for microseism generation and could affect H_s reconstructions. Alternatively, the time difference in peak energy may result from buoy 46013 being outside the local double-frequency microseism generation area that dominates the signal at BKS and for these northerly swell arrivals, R_s is somewhat smaller than that estimated by *Haubrich et al.* [1963].

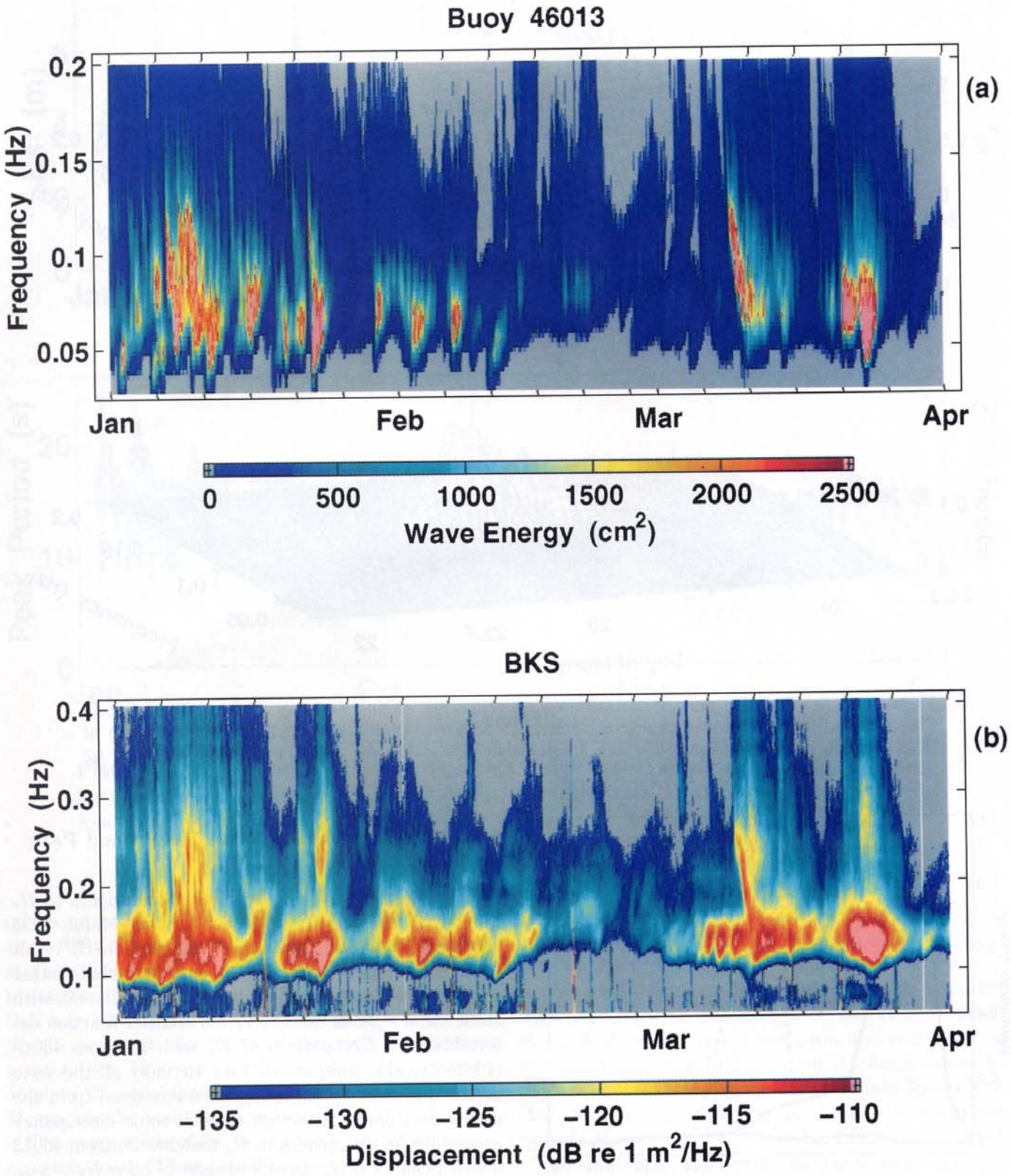

Plate 2. (a) Wave spectral energy at NOAA buoy 46013 for January-March 1995. (b) Microseism displacement spectral levels at Berkeley seismometer site (BKS) for January-March, 1995 (see Figure 1 for locations). Note that the frequency band shown is scaled to double that in Plate 2a.

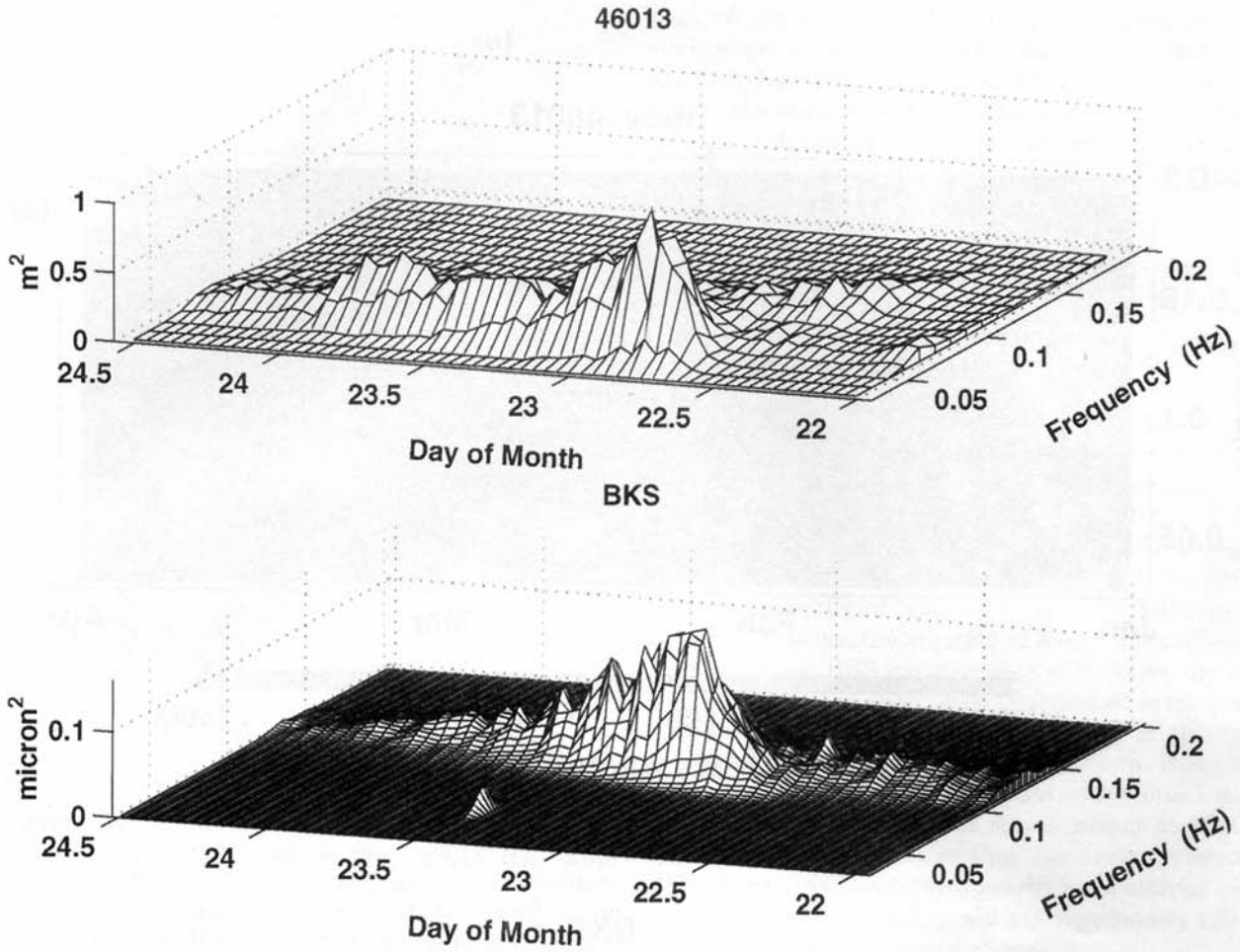

Figure 4. (a) Spectral energy variation of a swell event during January 22-24, 1995 (refer to Plates 2 and 3 for alternate characterizations). (b) Corresponding microseism energy levels at BKS for the same time period. The small ridge near noon on January 23 at 0.05 Hz is an earthquake surface-wave arrival.

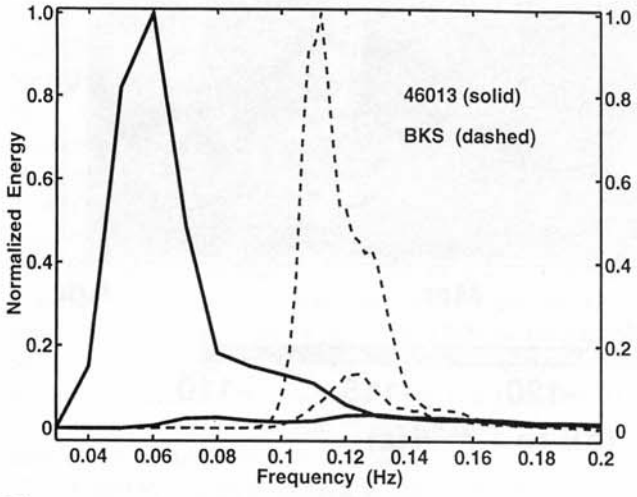

Figure 5. Normalized spectral energy at buoy 46013 (solid lines) and BKS (dashed lines) for the swell event shown in Figure 4. Top curves represent the peak energy at 2100 UT, and bottom curves represent the energy minimum preceding the swell arrival at 0600 UT on January 22. Each curve is normalized to the maximum spectral energy at 2100 UT on January 22 for their respective location.

5.3. Proxy Significant Wave Height and Peak Period

Application of the Γ_{sw} regression coefficients to $\hat{H}_s$ gives the reconstructed $\tilde{H}_s$ for January-March 1995 shown in Plate 3a (black line). The gaps in $\tilde{H}_s$ result from excluding those time periods that include either earthquake signals or other nonwave-related noise, with these same periods excluded from transfer function determination. Comparison of $\tilde{H}_s$ with H_s from 46013 (Plate 3a, blue line) shows that virtually all the wave events observed by the buoy were recovered from the microseism data. Although there is some discrepancy in amplitude, the pattern in $\tilde{H}_s$ matches H_s from 46013 nearly peak for peak. In all instances of buoy $H_s > 5$ m, the seismic reconstruction is consistently lower, making the $\tilde{H}_s$ a conservative estimate of H_s.

Comparing Plate 3a with Plate 2 shows that the largest differences between $\tilde{H}_s$ and H_s occur when there is significant wave energy at periods less than 10 s, e.g., on January 10 and March 10, which is associated with local storms. Part of this underestimation may result from the restriction of the upper limit of the seis-

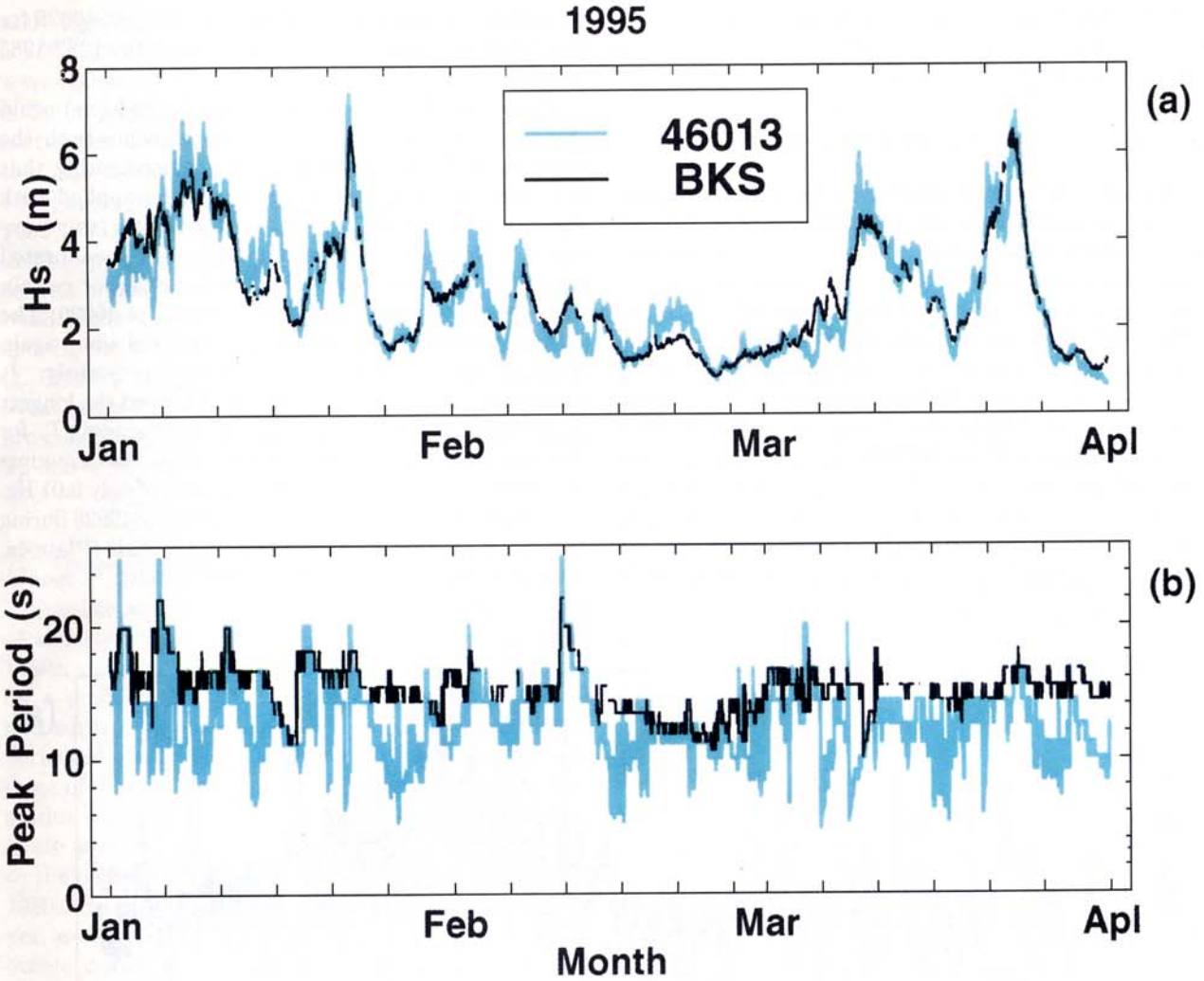

Plate 3. (a) Significant wave height H_s at NOAA buoy 46013 for January-March 1995 (blue line) and the seismic reconstruction (black line) from BKS ($\tilde{H}_s$) for the same time period. (b) Associated peak wave period T_p at 46026 and the corresponding reconstruction $\hat{T}_p$ from BKS.

mic band to 0.48 Hz. However, since there is generally little wave energy above 0.24 Hz, excluding energy at these frequencies should not significantly affect H_s reconstructions. For more regional and distant events that have similar characteristics along much of the California coast and where most of the energy is at periods greater than 12 s, e.g., the nearly 7 m H_s events on January 22 and March 23, the seismic reconstruction $\tilde{H}_s$ models the buoy H_s closely.

The comparison of the associated wave period reconstruction for 46013 and BKS is shown in Plate 3b. The reconstructed peak period $\hat{T}_p$ (black line) has a much narrower range and an obvious long-period bias. We note that buoy T_p measurements of low H_s long-period waves are subject to some uncertainty as a result of the nonlinear inversion from frequency to period and the potential for bimodal seas. Tests showed that the inversion results were not very sensitive to variation in estimates of either $\mathcal{W}_\theta$ or α_R, suggesting that some of the bias most likely results from the presence of telemicroseisms. When significant telemicroseism energy is present, $\hat{T}_p$ will have a long-period bias. An overestimation of T_p is more likely during low H_s when the telemicroseismic contribution to $\hat{S}_w$ can be more significant. Obliquely arriving swell will also contribute to the long-period bias in $\hat{T}_p$. Given the likely biases described above, close examination of Plate 3b suggests that, while the T_p match is not exact, the occurrence of high H_s long-period events (i.e., those events with $H_s > 5$ m and $T_p > 12$ s) can clearly be identified from the microseism data. In addition, Plate 3a shows that the presence of telemicroseism energy will not result in an overestimation of H_s for extreme wave events using the procedure given above.

These results indicate that the extreme wave climatology of the California coast can be accurately reconstructed from microseism data. In addition, these tests suggest a 3 month buoy deployment may obtain suf-

ficient wave measurements to satisfactorily calibrate a seismometer site, provided a sufficient number of high H_s events (i.e., $H_s > 5$ m) occur.

6. Application to El Niño 1997-1998

Recalling that our long-range goal is to investigate changes in the West Coast wave climate since 1930 using archived seismic data from BKS, it is important to demonstrate that the same Γ_{sw} transfer function determined for the BKS 1995 data can be applied to other BKS data with equally good recovery of H_s. Of interest is the comparison of the wave climate of the current strong ENSO with the strongest ENSO previously recorded, 1982-1983. Long-period seismometer data were obtained from NCEDC for BKS from November 1997 to March 30, 1998. Since buoy 46013 was out of service for much of this time, we show H_s from buoy 46026 (Plate 4) for comparison. Buoy 46026 was out of service during March, underscoring the usefulness of seismic reconstructions. Also shown is H_s at 46026 for the November-March time period during the 1982-1983 ENSO.

The proxy wave height $\tilde{H}_s$ (Plate 4a, red line) again displays a nearly one-to-one correspondence with the wave data (Plate 4a, black line), demonstrating that Γ_{sw} determined from 1995 data can be applied with equal success to BKS data from any year to reconstruct the coastal wave climate. Since Γ_{sw} is calibrated against deep water buoy 46013, seismic $\tilde{H}_s$ for certain wave events is greater than measured H_s at 46026. The reconstructed wave period (Plate 4b, red line) again displays the long-period bias observed previously. It should be noted that the difference between the longest T_p observed (25 s) and that of the corresponding T_p for the two long-period events in December 1997 amounts to a shift in the $\hat{S}_w$ spectral peak at BKS of only 0.01 Hz.

Comparison of the wave climate at buoy 46026 during the current ENSO with the 1982-1983 episode (Plate 4a, blue line) shows a generally similar pattern: a moder-

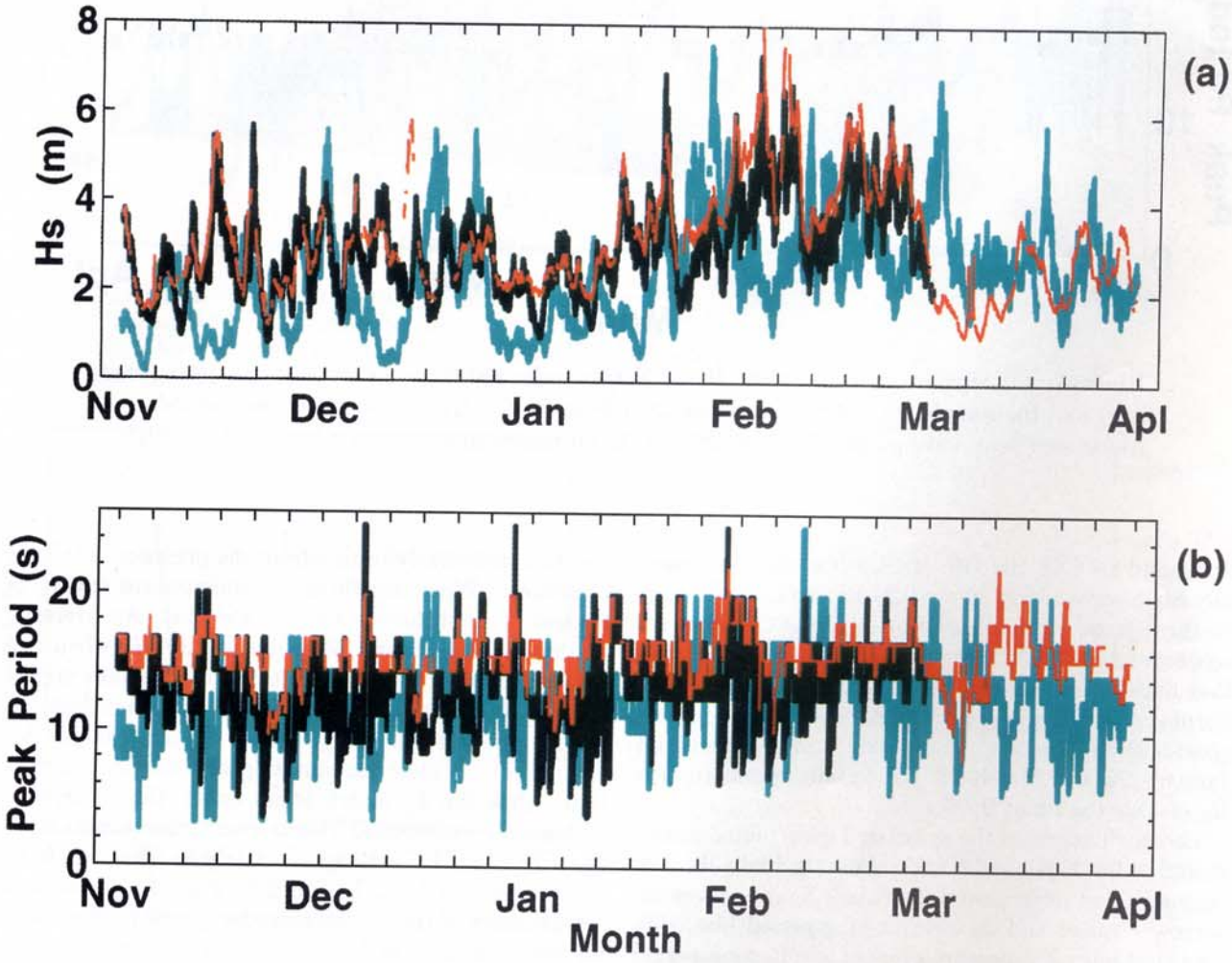

Plate 4. (a) Significant wave height at buoy 46026 for the 1982-1983 El Nino (blue line) and the 1997-1998 El Nino (black line). The seismic reconstruction $\tilde{H}_s$ (red line) from BKS microseism data for 1997-1998 using Γ_{sw} from 1995 compares favorably with the corresponding buoy data. (b) Corresponding peak wave period for the associated significant wave height data.

3, 1991, Honolulu, Hawaii, USA, ocean technologies and opportunities in the Pacific for the 90's, pp. 375-379, Inst. of Electr. and Electron. Eng., Piscataway, N. J., 1991.

Kibblewhite, A.C., and K.C. Ewans, Wave-wave interactions, microseisms, and infrasonic ambient noise in the ocean, *J. Acoust. Soc. Am.*, 78, 981-994, 1985.

Kibblewhite, A.C., and C.Y. Wu, The theoretical description of wave-wave interactions as a noise source in the ocean, *J. Acoust. Soc. Am.*, 89, 2241-2252, 1991.

Longuet-Higgins, M.S., A theory of the origin of microseisms, *Philos. Trans. R. Soc. London, Ser. A*, 243, 1-35, 1950.

Munk, W.H., G.R. Miller, F.E. Snodgrass, and N.F. Barber, Directional recording of swell from distant storms, *Philos. Trans. R. Soc. London, Ser. A*, 259, 505-584, 1963.

Nitta, T., and S. Yamada, Recent warming of tropical sea surface temperatures and its relationship to the northern hemisphere circulation, *J. Meteorol. Soc. Jpn.*, 67, 375-383, 1989.

Orcutt, J.A., C.S. Cox, A.C. Kibblewhite, W.A. Kuperman, and H. Schmidt, Observations and causes of ocean and seafloor noise at ultra-low frequencies, in *Natural Physical Sources of Underwater Sound*, edited by B. Kerman, pp. 203-232, Kluwer Acad., Norwell, Mass., 1993.

Pierson, W.J., Jr., and L. Moskowitz, A proposed spectral form for fully developed wind seas based on the similarity theory of S.A. Kitaigorodskii, *J. Geophys. Res.*, 69, 5181-5190, 1964.

Schmidt, H., and W.A. Kuperman, Estimation of surface noise source level from low-frequency seismoacoustic ambient noise measurements, *J. Acoust. Soc. Am.*, 84, 2153-2162, 1988.

Schreiner, A.E., and L.M. Dorman, Coherence lengths of seafloor noise: Effect of ocean bottom structure, *J. Acoust. Soc. Am.*, 88, 1503-1514, 1990.

Seymour, R.J., Wave climate variability in southern California, *J. Waterw. Port Coast. Ocean Eng.*, 122, 182-186, 1996.

Seymour, R.J., R.R. Strange III, D.R. Cayan, and R.A. Nathan, Influence of El Niños on California's wave climate, in *Nineteenth Coastal Engineering Conference, Proceedings of the International Conference, September 3-7, 1984, Houston, Texas*, edited by B.L. Edge, pp. 577-592, Am. Soc. of Civ. Eng., New York, 1984.

Steele, K.E., J.C. Lau, and Y.L. Hsu, Theory and application of calibration techniques for an NDBC directional wave measurements buoy, *IEEE J. Oceanic. Eng.*, 10, 382-396, 1985.

Tillotson, K., and P.D. Komar, The wave climate of the Pacific Northwest (Oregon and Washington): A comparison of data sources, *J. Coastal Res.*, 13, 440-452, 1997.

Trenberth, K.E., Recent observed interdecadal climate changes in the northern hemisphere, *Bull. Am. Meteorol. Soc.*, 71, 988-993, 1990.

Trenberth, K.E., and J.W. Hurrell, Decadal atmosphere-ocean variations in the Pacific, *Clim. Dyn.*, 9, 303-319, 1994.

Webb, S.C., The equilibrium oceanic microseism spectrum, *J. Acoust. Soc. Am.*, 92, 2141-2158, 1992.

Webb, S.C., Broad-band seismology and noise under the ocean, *Rev. Geophys.*, 36, 105-142, 1998.

Webb, S.C., and C.S. Cox, Observations and modeling of sea floor microseisms, *J. Geophys. Res.*, 91, 7343-7358, 1986.

Zopf, D.O., H.C. Creech, and W.H. Quinn, The wavemeter: A land-based system for measuring nearshore ocean waves, *Mar. Technol. Soc. J.*, 10, 19-25, 1976.

P. D. Bromirski and R. E. Flick, Center for Coastal Studies, 0209, Scripps Institution of Oceanography, University of California, 8602 La Jolla Shores Drive, La Jolla, CA 92037. (e-mail: peter@coast.ucsd.edu, ref@coast.ucsd.edu)

N. Graham, Climate Research Division, 0235, Scripps Institution of Oceanography, University of California, 8602 La Jolla Shores Drive, La Jolla, CA 92037. (e-mail: graham@grace.ucsd.edu)

(Received July 20, 1998; revised March 9, 1999; accepted April 15, 1999.)